Large Eddy Simulation of Ducted Propulsors in Crashback

Hyunchul Jang, Krishnan Mahesh

(Aerospace Engineering and Mechanics, University of Minnesota)

ABSTRACT

Flow around Propeller 4381 with duct is computed with the large eddy simulation methodology during crashback condition. A non-dissipative robust numerical algorithm developed by Mahesh et al. (2004) for unstructured grids is used. The ducted propeller without stator blades is solved in a rotating frame of reference. The flow is computed up to about 86 revolutions at the advance ratio J=-0.7 and Re=480,000 based on the propeller diameter. These preliminary results are discussed. The simulation shows that the evolutions of the thrust and torque are highly unsteady and have low frequency fluctuations. The computed mean values of the unsteady load are more negative as compared to the experimental results. Absence of the stator blades is thought to be responsible. The unsteady loads on the duct are also measured. Even though the effect of the duct on K_T and K_Q are not very large, that on the side force is significant. The effect of viscous force on the total unsteady loads is considered and the results indicate that the pressure load is dominant. The computed circumferential average of mean and RMS of velocity are compared to experimental results. Pressure distributions on blade surfaces and duct surface are also discussed.

INTRODUCTION

Crashback is an operating condition where the propeller rotates in the reverse direction while the vessel moves in the forward direction. Since the crashback condition is dominated by large scale unsteadiness, it is well known as one of the most challenging to analyze. Low frequency components of the unsteadiness can affect propeller thrust, torque, and side-forces, which are related to maneuverability of the vessel during crashback condition.

The crashback condition is dominated by the interaction of the free stream flow with the strong reversed flow from propeller rotation as shown in figure 1(a). This interaction forms the unsteady ring vortex that is the most remarkable aspect of the flow
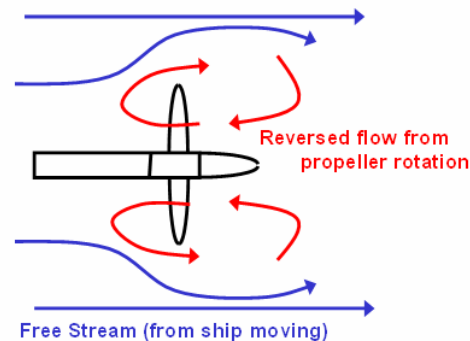

Figure 1: Schematic of crashback condition.

during crashback operation.

Jiang et al. (1996) studied the structure of the unsteady vortex ring using PIV measurements. They noted that the unsteady ring vortex is related to the unsteady shaft forces and the oscillation frequency of the ring vortex is much lower than the propeller rotation rate. Jessup et al. (2004) present more detailed measurements of the flow velocity field using PIV and LDV.

The computational prediction of the flow around marine propellers has been performed using unsteady Reynolds-Averaged Navier-Stokes equations (RANS) (Chen & Stern, 1999; Davoudzadeh et al., 1997). They show that RANS yields good results for forward mode and backward mode, but yields the significant discrepancy in crashback mode and crashahead mode. Vyšohlíd & Mahesh (2006) showed that the Large Eddy Simulation (LES) yields good agreement for mean values of thrust and torque in crashback mode. Their simulations show the presence of the ring vortex and low frequency unsteadiness in thrust, torque and side forces.

The above studies were for open propellers. In

order to investigate the effect of the duct on the crashback performance, experiments using various devices were performed with and without the duct by Jessup et al. (2006). This paper performs LES of ducted propulsor in crashback.

SIMULATION DETAILS

Propeller Geometry

The computations are performed for marine propeller P4381, which is a five-bladed, right-handed with variable pitch, no skew and rake. The propeller has been used in various experiments (Jessup et al., 2004; Jessup et al., 2006; Jiang et al., 1997) and computations (Chen & Stern, 1999; Davoudzadeh et al., 1997; Vyšohlíd & Mahesh, 2006). The detailed propeller geometry and hub geometry are given in Jessup et al. (2006). To investigate the effect of a duct, a neutrally loaded duct was designed to fit around P4381. Figure 2(a) shows the illustration of the originally designed ducted propeller, which also has 12
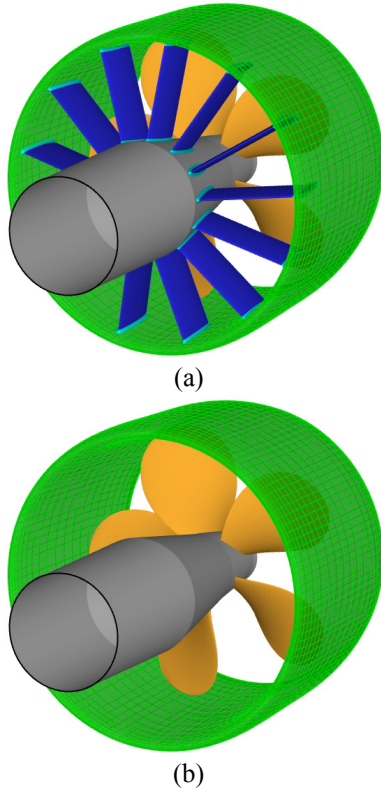

(a)

(b)

Figure 2: The geometries of ducted propellers with and without stator blades (a) the originally designed ducted propeller with stator blades, (b) the ducted propeller without stator blades.

stator blades in the upstream of rotor blades.

Numerical Methods

We solve for the flow around the ducted propeller in a rotating frame of reference. When some solid boundaries are rotating and the others are stationary, the rotating frame of reference method requires the stationary parts to be axy-symmetric. The ducted propeller given in figure 2(a) has a rotating hub with five blades and the other stationary parts such as stationary shaft, duct, and stator blades. Even though the shaft and the duct are axi-symmetric, the stator blades are not axi-symmetric. Thus, the ducted propeller with stator blades cannot be solved in the rotating frame of reference so that a modified version of the ducted propeller without stator blades are suggested as shown in figure 2(b). The computations in this study used the modified ducted propeller without stator blades.

The incompressible Navier-Stokes equations in a rotating frame of reference can be formulated in a strongly conservative form without the traditional source term, such as the Coriolis and centrifugal forces (Beddhu et. al., 1996). Furthermore, the equations can be rewritten with the velocity vector in the absolute frame. The governing equations in the strong conservative form in a rotating frame of reference are in a tensor notation as follows.

$$\frac{\partial u_i}{\partial t} + \frac{\partial}{\partial x_j}(u_i u_j - u_i \varepsilon_{jkl}\omega_k x_l) =$$
$$-\frac{\partial p}{\partial x_i} - \varepsilon_{ijk}\omega_j u_k + v\frac{\partial^2 u_i}{\partial x_j \partial x_j} \quad (1)$$
$$\frac{\partial u_i}{\partial x_i} = 0$$

where u_i are the inertial velocities in the absolute frame, p is the pressure, x_i are coordinates in the rotating non-inertial reference frame, ω_j is the angular velocity of the rotating frame of reference, v is the kinematic viscosity, and ε_{ijk} denotes the permutation symbol for the tensor notation.

In LES, the larger unsteady motions are directly solved with spatially filtered equations, whereas the effects of the smaller scale motions are modeled. and models the sub-grid stress The spatially filtered momentum equation in the initial reference frame is

$$\frac{\partial \overline{u_i}}{\partial t} + \frac{\partial}{\partial x_j}(\overline{u_i u_j}) = -\frac{\partial \overline{p}}{\partial x_i} + \nu \frac{\partial^2 \overline{u_i}}{\partial x_j \partial x_j} - \frac{\partial \tau_{ij}}{\partial x_j} \qquad (2)$$

$$\frac{\partial \overline{u_i}}{\partial x_i} = 0$$

where $\overline{}$ denotes the spatial filter and $\tau_{ij} = \overline{u_i u_j} - \overline{u_i}\,\overline{u_j}$ is the sub-grid stress. The sub-grid stress is modeled with dynamic Smagorinski model (Germano et al., 1991; Lilly, 1992).

In the rotating frame of reference, we have the additional rotational term in the filtered equations as we've done before.

$$\frac{\partial \overline{u_i}}{\partial t} + \frac{\partial}{\partial x_j}(\overline{u_i u_j} - \overline{u_i}\varepsilon_{jkl}\omega_k x_l) =$$

$$\qquad -\frac{\partial \overline{p}}{\partial x_i} - \varepsilon_{ijk}\omega_j \overline{u_k} + \nu \frac{\partial^2 \overline{u_i}}{\partial x_j \partial x_j} - \frac{\partial \tau_{ij}}{\partial x_j} \qquad (3)$$

$$\frac{\partial \tilde{u_i}}{\partial x_i} = 0$$

with an approximation $\overline{u_i \varepsilon_{jkl}\omega_k x_l} \approx \overline{u_i}\varepsilon_{jkl}\omega_k x_l$.

The above equations are solved using a numerical method developed by Mahesh et al. (2004) for incompressible flows on unstructured grids. The algorithm is derived to be robust without numerical dissipation. It is a finite volume approach which stores the Cartesian velocities and the pressure at the centroids of the cells and the face normal velocities are stored independently at the centroids of the faces. A predictor-corrector approach is used. The predicted velocities at the control volume centroids are first obtained and then interpolated to obtain the face normal velocities. The predicted face normal velocity is projected so that continuity is discretely satisfied. This yields a Poisson equation for pressure which is solved iteratively using a multigrid approach. The pressure field is used to update the Cartesian control volume velocities using a least-squared formulation. Time advancement is implicit and is performed using the Crank-Nicolson scheme. The algorithm has been validated for a variety of problems (Mahesh et al., 2004) over a range of Reynolds numbers

Computational Mesh and Boundary Conditions

The computational domain is a cylinder with the diameter of 7.0D and the length of 14.0D where D is the diameter of the propeller disk. Free-stream velocity boundary conditions are specified at the inlet and the lateral boundaries. Convective boundary conditions are prescribed at the exit. As mentioned, boundary conditions on solid walls are forced as those are prescribed in the inertial reference frame. That is to say, boundary conditions on rotor part, blades and hub, are specified with $u = \omega \times r$, while those on stator part, shaft and duct are prescribed with no-slip boundary conditions. Schematics of the computational domain and boundary conditions are shown in figure 3(a) and 3(b).

Gambit and TGrid (Fluent corp.) are used for grid generation. Tetrahedral meshes are used near the propeller to match the complex geometry of blades and duct. The tetrahedral meshes are restricted to near the propeller and hexahedral and prism meshes are extended from the tetrahedra to the boundary of the domain. Four layers of prisms are grown from the surfaces of blades, hub, and shaft and three layers of prisms are also grown from the duct surface in order to resolve the boundary layer on the surfaces. The
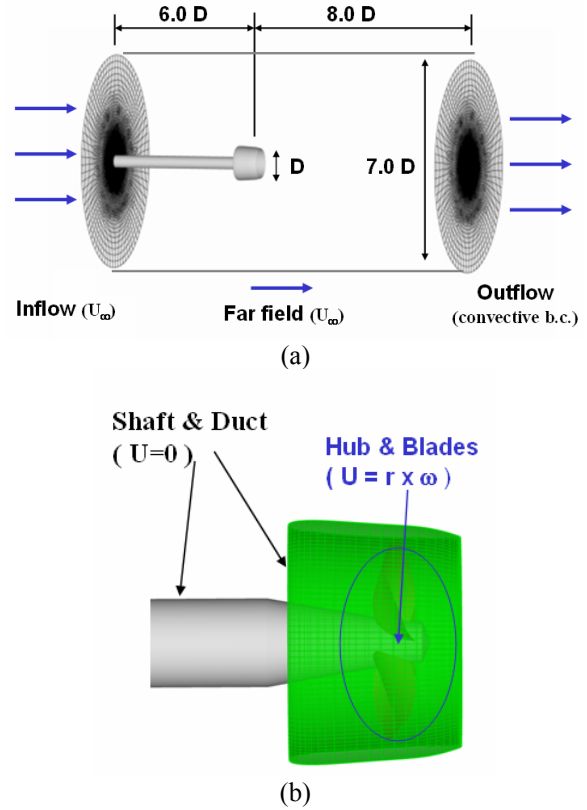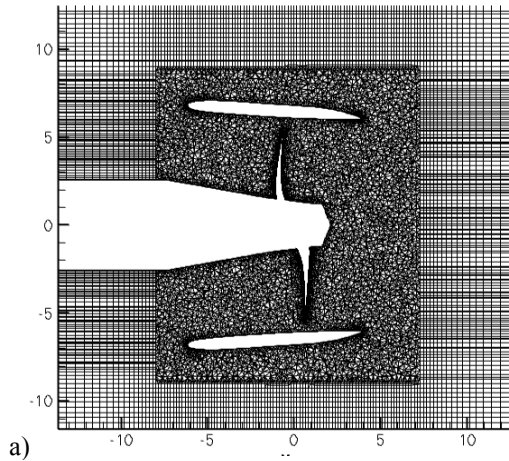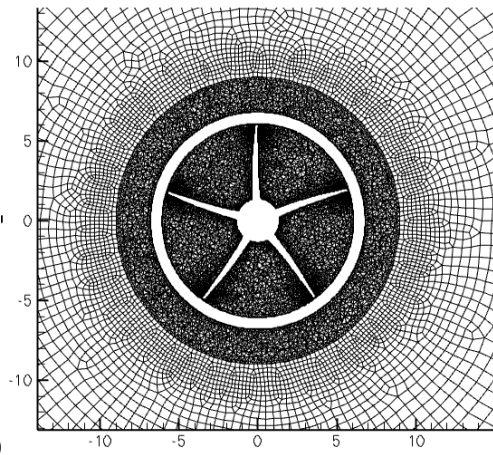

(a)

(b)

Figure 3: (a) Computational domain and boundary conditions on domain boundaries, (b) boundary conditions on solid walls.

**Figure 4**: The computational mesh in cross-sections: (a) XY plane, (b) YZ plane.

computational meshes in the propeller neighborhood are shown in figure 4(a) and 4(b). The inner zone that looks very dense in figure 4 consists of tetrahedral elements, while the outer zone is composed of hexahedral and prism elements. The total number of the computational meshes is about 19 million, which is partitioned among 512 processors.
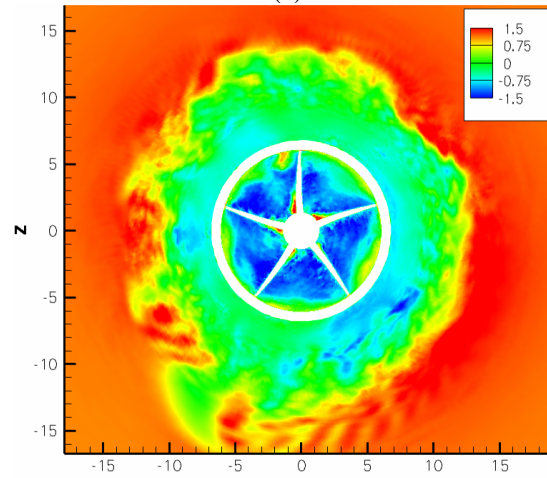
RESULTS

The advance ratio J and Reynolds number *Re* are defined by

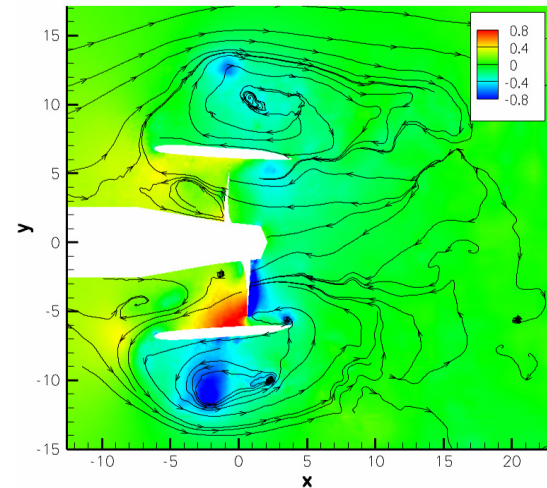$$J = \frac{U}{nD}, \quad \text{Re} = \frac{DU}{\nu} \tag{4}$$

where U is the free-stream velocity, n is the propeller rotational speed, and D is the diameter of the propeller
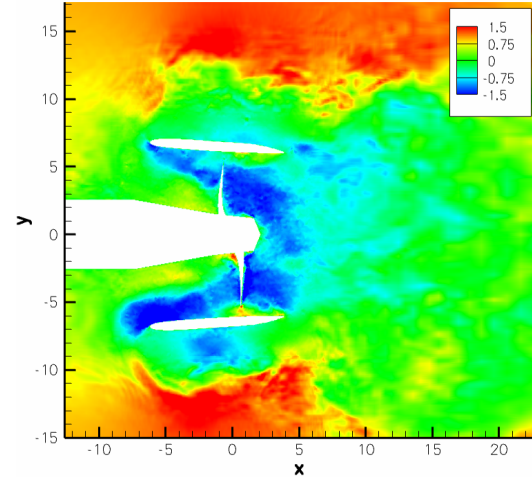
Figure 5: Contours of instantaneous flow variables at 86 revolutions: (a) axial velocity in XY plane at z/D=0, (b) axial velocity in YZ plane at x/D=0, (c) pressure in XY plane at z/D=0 with streamlines.

disk.

Simulations were performed in the crashback mode at the advance ratio J = -0.7 for which unsteady loads were measured in a 36 inch water tunnel and flow fields were captured with LDV and PIV by Jessup et al. (2004 and 2006). The Reynolds number of the simulation was 480,000.

The computation has been advanced up to 86 revolutions. The number of revolutions is not large enough as compared to previous experiments (Jessup et al., 2004, 2006) and computations (Vyšohlíd and Mahesh, 2006). The experiments were performed for 700 revolutions and even the computation was performed over 300 revolutions. The present results are therefore preliminary.
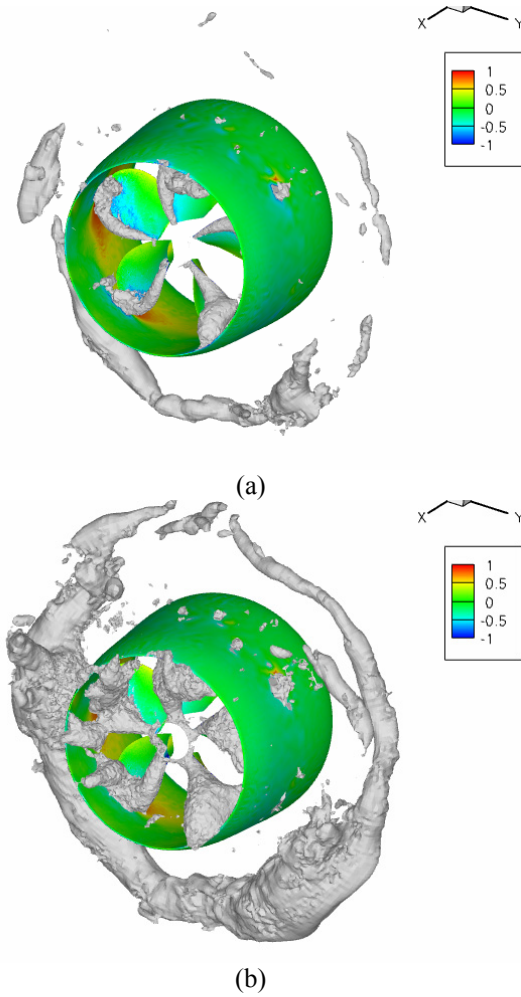

(a)

(b)

Figure 6: Iso-surfaces of constant low pressure, illustrating the existence of the propeller vortex ring: (a) at p=-0.33, (b) at p=-0.29.

Instantaneous contours of axial velocities and pressure are shown in figure 5. Figure 5(a) and 5(b) provides cross-sections of the flow by XY plane at z/D=0 and YZ plane at x/D=0, respectively. The direction of free stream flow is from left to right while the propeller propels the flow from right to left. The red colored outer region represents the free-stream and the blue colored inner region represents the strong reversed flow induced by the propeller rotation. Those two opposite directional flows creates a recirculation zone that is denoted by green colored region. Pressure contour with streamlines in figure 5(c) more clearly shows the existence of the asymmetric irregular recirculation zone, which is called a propeller ring vortex. The centers of vortices beyond and below the duct are located in the local minimum of pressure.

The three dimensional structure of the vortex ring can be visualized by plotting an iso-surface of constant low pressure in figure 6(a) and 6(b). Pressure contours are plotted on the surfaces of blades and the duct and grey shaded structures are the iso-surface illustrating the ring vortex. This figure shows the asymmetry and irregularity of the vortex ring better than the cross-sectional plots.

Time History of Unsteady Loads

The axial component of force is the thrust *T* and the axial component of moment of force is the torque *Q*. In addition, a projection of force onto the direction perpendicular to the propeller axis is termed the side force. Since computations are performed in the rotating frame of reference, the side force is translated to the inertial reference frame. The horizontal and vertical components of the side force, F_H and F_V, respectively, can be obtained from a rotational transformation using the angle between the rotating frame and the inertial frame.
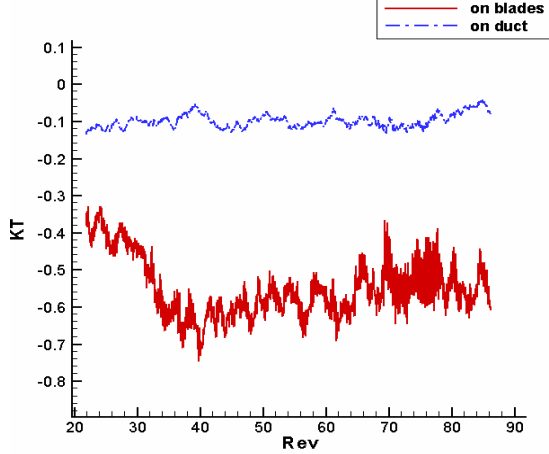
Non-dimensional thrust coefficient K_T, torque coefficient K_Q, side force coefficient K_F and side force angle θ_F are given by

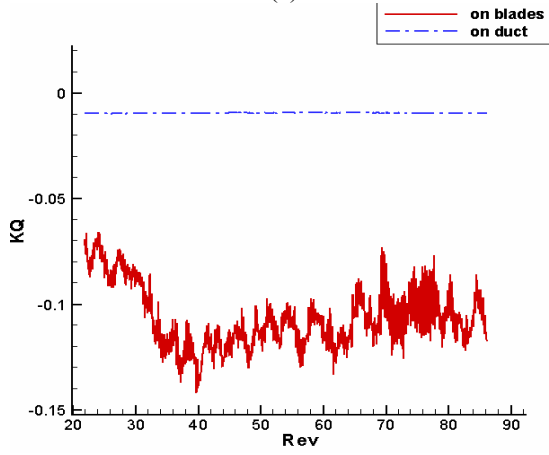$$K_T = \frac{T}{\rho n^2 D^4}, \quad K_Q = \frac{Q}{\rho n^2 D^5} \qquad (5)$$

$$K_F = \frac{\sqrt{F_H^2 + F_V^2}}{\rho n^2 D^4}, \quad \theta_F = \tan^{-1}(\frac{F_V}{F_H}) \qquad (6)$$

where ρ is the density of the fluid, *n* is the propeller rotational speed, and *D* is the diameter of the propeller disk.

The time histories of K_T and K_Q are shown in figure

(a)

(b)

Figure 7: Time history of thrust coefficient K_T and torque coefficient K_Q on the surfaces of blades and the duct: (a) time history of K_T, (b) time history of K_Q.

	$<K_T>$	$(K_T)'$	$<K_Q>$	$(K_Q)'$
LES on all	-0.63	0.079	-0.117	0.014
LES on blade	-0.55	0.079	-0.107	0.014
LES on duct	-0.097	0.018	-0.0093	1.3e-4
WT (2006)	-0.38		-0.078	

(a) Results of ducted propellers

	$<K_T>$	$(K_T)'$	$<K_Q>$	$(K_Q)'$
LES (2006)	-0.39	0.068	-0.073	0.012
WT (2004)	-0.33	0.060	-0.065	0.011
OW (2006)	-0.41		-0.078	
OW (2004)	-0.50		-0.093	

(b) Results of open propellers

	$<K_{Tv}>$	$(K_{Tv})'$	$<K_{Tp}>$	$(K_{Tp})'$
LES on all	1.8e-4	3.9e-4	-0.63	0.079
LES on blade	9.3e-4	9.3e-4	-0.55	0.079
LES on duct	8.6e-4	2.2e-4	-0.097	0.018

(c) Contributions of viscous force or pressure to K_T

Table 1: Mean and RMS values of the thrust coefficient K_T and torque coefficient K_Q : (a) results of ducted propellers, (b) results of open propellers, (c) contributions of viscous force or pressure to K_T.
  WT means 36" water tunnel experiment and OW is towing tank experiment by Jessup et al. (2004, 2006). LES(2006) is the open propeller computation by Vysohlid & Mahesh (2006).
  K_{Tv} is from viscous force and K_{Tp} is from pressure.

7(a) and 7(b), respectively. The red solid line represents each coefficient on blade surfaces and blue dashed line corresponds to the duct surface. This decomposition of loads can help us understand the effect of duct force. Both the thrust and the torque on blades show similar tendency with low frequency and large amplitude of fluctuations. However, K_T on the duct is smaller than K_T on blades and K_Q on the duct appears negligible.

Table 1 compares computed mean and RMS values of thrust coefficient K_T and torque coefficient K_Q to the experimental results. $< \cdot >$ denotes mean value and $(\cdot)'$ denotes RMS value. Table 1(a) shows results of ducted propellers and table 1(b) are results of open propeller in order to see the difference between results of LES and experiments.

In the table, WT denotes 36″-water tunnel experiments. Since the size of the water tunnel is, however, only three times of propeller diameter, it may suffer from tunnel effect. Particularly, the ring vortex structure caused by crashback could interact with the tunnel surface due to the insufficient size of the water tunnel. On the other hands, towing-tank experiment denoted by OW does not have any tunnel effect, but only unsteady load in the axial direction are measured in the experiment. According to the experiments, the effect of the duct for the unsteady loads is slightly more negative thrust and torque. However, the computed mean values of the unsteady load are quite more negative as compared to the experimental results. One possible reason for the discrepancy is the insufficient number of rotations and another possibility is the absence of the blocking effect of stator blades.

Table 1(c) shows how much viscous forces and pressure contribute to the total thrust. The results show that the thrust due to pressure is dominant. So, pressure distribution on the surfaces is very important to understand the character of the unsteady loads.

Table 2 provides a comparison of side force coefficients from computations and experiments. The computed mean side force coefficient, denoted by $<K_F>$, on the blade surfaces is quite similar to the value from the experiment. As Jessup et al. (2006) mentions, $<K_F>$ on the blade surfaces does not change with the existence of the duct. However, $<K_F>$ on the duct surface was not measured in Jessup et al.'s experiment. The computational results note that $<K_F>$ on the duct surface make a primary contribution to the total $<K_F>$, so that the total $<K_F>$ is about 5 times larger than $<K_F>$ on blades surfaces. This trend is clearly shown in figure 8(a). The blue dotted line representing $<K_F>$ on the duct overwhelms the red solid line representing $<K_F>$ on the blades. As explained before, pressure loads are dominant in the total unsteady loads so that the unsteady loads on a surface element are given by the dot product of the surface normal vector and the pressure. Since most of normal vectors on the duct are almost normal to the axial direction and those on blades are nearly parallel to the axial direction, $<K_F>$ on the duct may be large even though $<K_T>$ and $<K_Q>$ on the duct are relatively small.

Figure 8(b) shows time history of the angle of the side force on the all surfaces, blades, and the duct. The figure indicates that the angle of the side force on all surfaces follows that on the duct and it is very periodic. It may be because the side force from the duct is dominant. The period of the total side force is about a half revolution. The non-dimensional rotating frequency of the side force f_s is defined by

$$f_S = \frac{\omega_S D}{U} \qquad (7)$$

where ω_s is the angular velocity of the side force.

Since the period of the side force is a half revolution, the ω_s is 2ω. Thus, the non-dimensional rotating frequency of the side force $f_s = 0.125$.

Time Average of Flow Fields

The computed results are averaged circumferentially and in time over a period of 64.28 revolutions time from 21.79 revolutions to 86.08 revolutions. The averaged fields are compared with corresponding experimental results of Jessup et al. (2006).
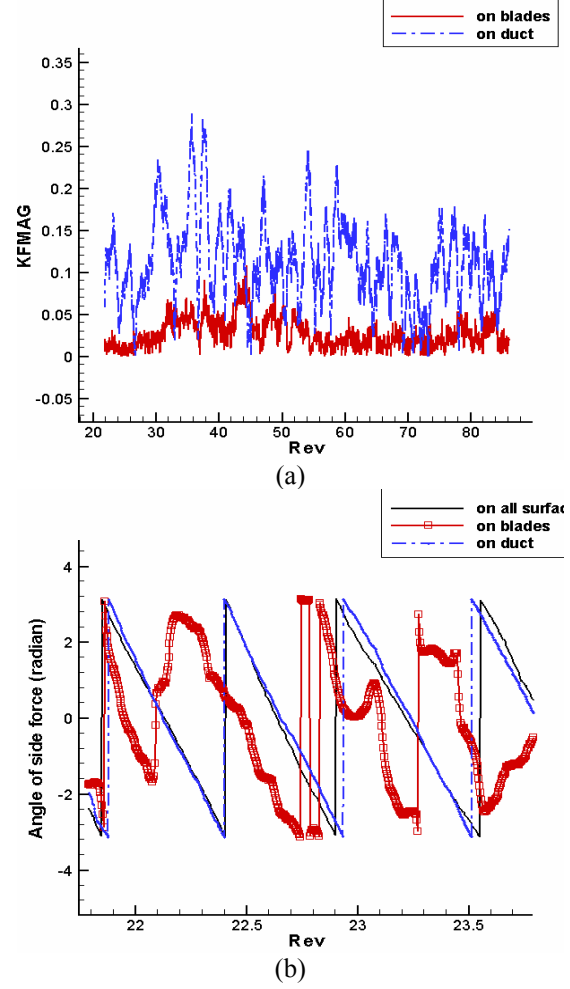

(a)

(b)

Figure 8: (a) Time history of the side force coefficient K_F on the surfaces of blades and the duct, (b) The angle of side force on the surfaces of blades and the duct.

	$<K_F>$	$(K_F)'$
LES on all	0.14	0.062
LES on blade	0.027	0.017
LES on duct	0.11	0.050
WT (2006)	0.024	

(a) Results of ducted propellers

	$<K_F>$	$(K_F)'$
LES (2006)	0.025	
WT (2004)	0.024	

(b) Results of open propellers

Table 2: Mean and RMS values of non-dimensional side force K_F : (a) results of ducted propellers, (b) results of open propellers.

Contours of averaged axial velocity with streamlines are plotted in figure 9(a). Blue colored zone in the neighborhood of blades means strongly reverse flow from propeller rotation. This reverse flow interacts with surrounding free stream to create a recirculation zone outside of the duct. The effect of the duct is to move the center of the recirculation zone outboard as Jessup et al. (2006) note.

Figure 9(b) and 9(c) compare computed and measured RMS contours of radial velocity. The computed and measured data show reasonable good agreement, but the center of computed ring vortex is somewhat closer to the propeller blades than that of measured ring vortex

Pressure on Blades and duct Surfaces

The pressure distribution on the blade surfaces and the duct surface was examined. The maximum and minimum of the pressure are observed in the neighborhood of thinner edges of the blades. These thinner edges act as leading edges in crashback.

The contours of instantaneous pressure on propeller surfaces are shown in figure 10(a) and 10(b). Figure 10(a) and 10(b) are downstream side of view and upstream side view, respectively. These figures note that the former is the suction side of blades and the latter is the pressure side of blades.

Figure 11(a)-(c) show contours of averaged pressure with streamlines in the cross-plane at a constant radius. The flow is move from right to left with high angle of attack. At r/R=0.3 in figure 11(a), the flow is detached on the middle of the suction side. On the other hands, the flows are still attached along both sides at r/R=0.5 and 0.7.

The effect of the duct is to move the center of the recirculation zone outboard as Jessup et al. (2006) mentioned. Also, the flow is attached to both the inside and outside duct surface. However, the center of the recirculation zone from the experimental data is located more down-stream than that from the computed data.

Figure 12(a) and 12(b) show contours of instantaneous pressure on the inner surface of the duct and the outer surface of the duct, respectively. Even though unsteady fluctuations also exist on the outer surface, the level of the pressure is relatively lower. On the inner surface, the pressure fluctuations are more prominent. The local high pressure and low pressure regions are located in the vicinity of blade tips. The local high pressure region comes from the pressure side of the blade and the local low pressure region is from
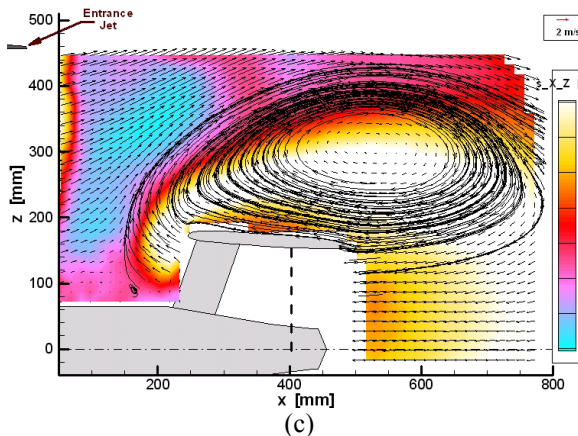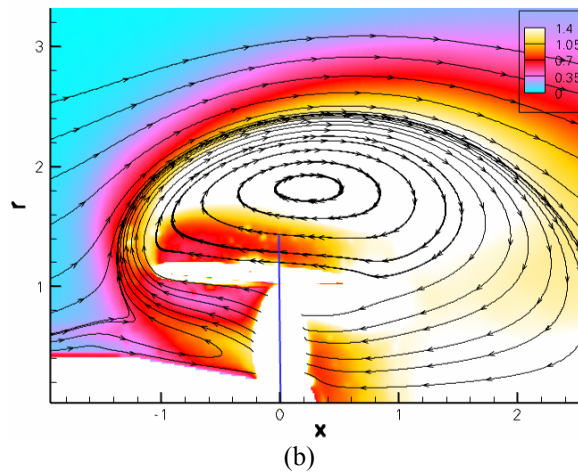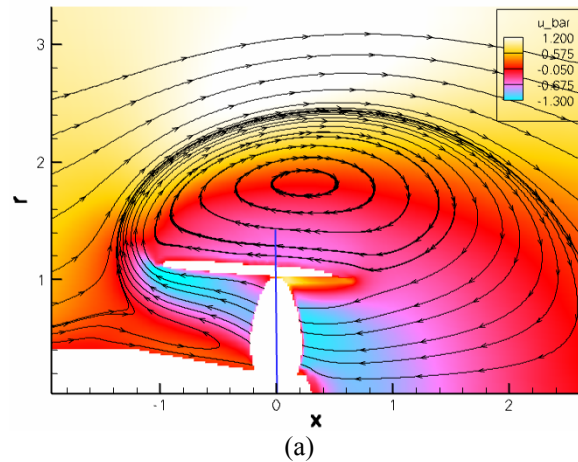

(a)

(b)

(c)

Figure 9: Contours of circumferentially and timely averaged field with streamlines: (a) averaged axial velocity from computation, (b) RMS of radial velocity from computation, (c) RMS of radial velocity from experiment (Jessup et al., 2006).
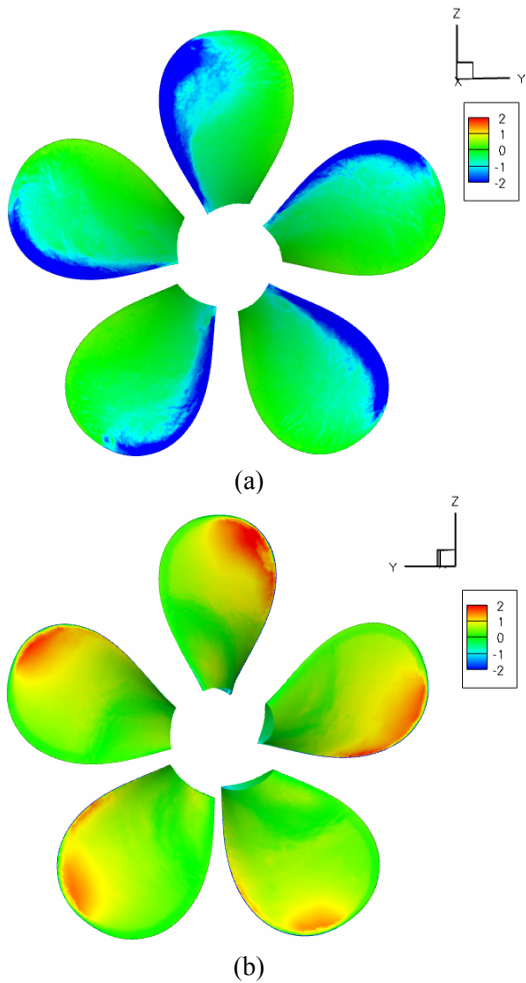
(a)

(b)

Figure 10: Contours of instantaneous pressures with streamlines on blade surfaces: (a) downstream side view (suction side) , (b) upstream side view (pressure side).

the suction side of the blade. These local high and low pressure region are possibly why the magnitude of the side force on the duct is quite large.

CONCLUSIONS

Flow around ducted propeller 4381 in crashback is simulated with the large eddy simulation methodology . The ducted propeller without stator blades is computed with the strongly conservative formulation of the rotating frame of reference as a simpler version of the ducted propeller. The ducted propeller is computed up to about 86 revolutions on a 19 millions computational mesh at the advance ration J=-0.7 and Re=480,000.

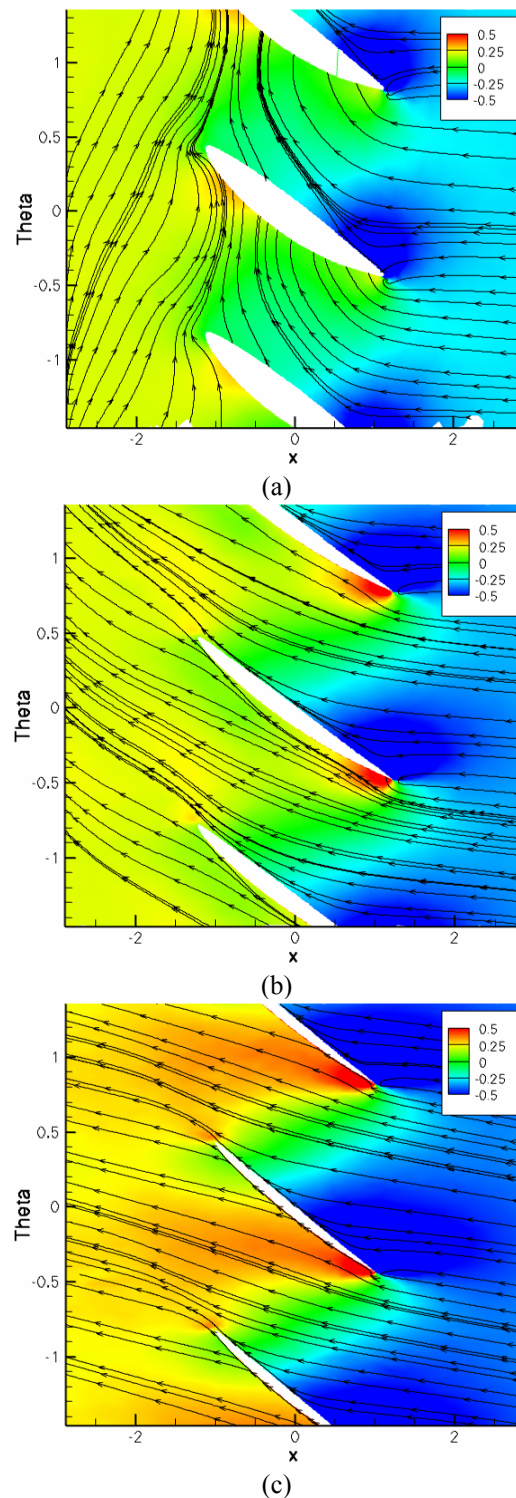The simulation shows that the highly unsteady thrust and torque have low frequency fluctuations. The

(a)

(b)

(c)

Figure 11: Contours of averaged pressure on blade sections with streamlines: (a) at r/R=0.3, (b) at r/R=0.5, (c) at r/R=0.7.

computed mean values of the unsteady load are more negative than the experimental results. Absence of the stator blades is thought to be responsible. The unsteady loads on the duct are also measured. Even though the effect of the duct for K_T and K_Q are not very large, that for the side force is significant. The effect of viscous force on the total unsteady loads is considered and the results indicate that the pressure load is dominant. The computed circumferential average of mean and RMS of velocity are compared to experimental results. Pressure distributions are also discussed on blade surfaces and duct surface.

(a)   (b)

Figure 12: Contours of instantaneous pressure field: (a) on the outer surface of duct, (b) on the inner surface of duct.

REFERENCES

Beddhu, M., Taylor, L. K., Whitfield, D. L., "Strong Conservative Form of the Incompressible Navier-Stokes Equations in a Rotating Frame with a Solution Procedure", Journal of Computational Physics, Vol. 128, 1996, pp. 427-437.

Chen, B., Stern, F., "Computational Fluid Dynamics of Four Quadrant Marine Propulsor Flow", Journal of Ship Research, Vol. 43, No. 4, 1999, pp. 218-228.

Davoudzadeh, F., Taylor, L. K., Zierke, W. C., Dreyer, J. J., McDonald, H., Whitfield. D. L., "Coupled Navier-Stokes and Equations of Motion Simulation of Submarine Maneuvers, Including Crashback", Proceedings of the 1997 ASME Fluids Engineering Division Summer Meeting, Vol. 2, ASME, New York, 1997.

Germano, M., Piomelli, U., Moin, P., Cabot, W. H., " A dynamic Subgrid-Scale Eddy Viscosity Model", Physics of Fluids A, Vol. 3, No. 7, 1991, pp. 1760-1765.

Jiang, C. W., Dong, R. R., Lui, H. L., Chang, M. S., "24-inch Water Tunnel Flow Field Measurements During Propeller Crashback", 21st Symposium on Naval Hydrodynamics, The National Academies Press, Washington, DC, 1997, pp. 136-146.

Jessup, S., Chesnakas, C., Fry, D., Donnelly, M., Black, S., Park, J., "Propeller Performance at Extreme Off Design Conditions", Proceedings of the 25th Symposium on Naval Hydrodynamics, St. John's, Canada, August 2004.
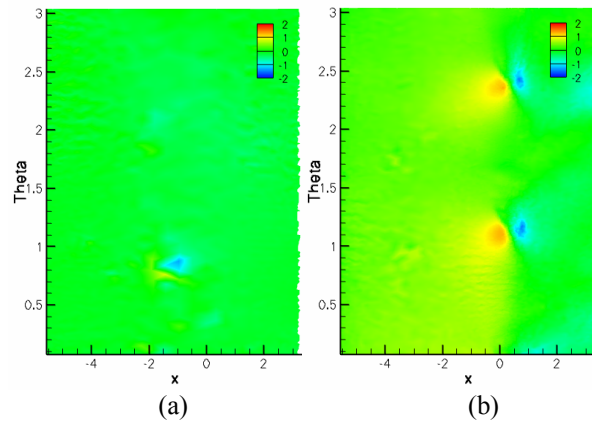
Jessup, S., Fry, D., Donnelly, M., "Unsteady Propeller Performance in Crashback Conditions With and Without Duct", Proceedings of the 26th Symposium on Naval Hydrodynamics, Rome, Italy, September 2006.

Lilly, D. K., " A Proposed Modification of the Germano Subgrid-Scale Closure Model", Physics of Fluids A, Vol. 4, No. 3, 1992, pp. 633-635.

Mahesh, K., Constantinescu, G., Moin, P., "A Numerical Methods for Large-Eddy Simulation in Complex Geometries", Journal of Computational Physics, Vol. 197, No. 1, 2004, pp. 215-240.

Vyšohlíd, M., Mahesh, K., "Large Eddy Simulation of Crashback in Maring Propellers", Proceedings of the 26th Symposium on Naval Hydrodynamics, Rome, Italy, September 2006.